Optics and Laser Technology, Volume 101, May 2018, pp. 1-10
DOI:10.1016/j.optlastec.2017.10.027

Porphyrin-Nanoassembled Fiber-Optic Gas Sensor Fabrication: Optimization of Parameters for Sensitive Ammonia Gas Detection

Sergiy Korposh[2], Suguru Kodaira[1], Roman Selyanchyn[1], Francisco H. Ledezma[1], Stephen W. James[3], and Seung-Woo Lee[1,4]*

[1] Graduate School of Environmental Engineering, The University of Kitakyushu, 1-1 Hibikino, Wakamatsu, Kitakyushu 808-0135, Japan.
[2] Department of Electrical and Electronic Engineering, University of Nottingham, Nottingham, NG7 2RD, UK.
[3] Centre for Engineering Photonics, Cranfield University, Cranfield, Bedford MK43 0AL, UK.
[4] EnH Japan Co. Ltd., 1-103 Hibikinokita, Wakamatsu, Kitakyushu 808-0137, Japan.

* Correspondence: leesw@kitakyu-u.ac.jp; Tel.: +81-93-695-3293; Fax: +81-93-695-3384

Abstract

Highly sensitive fiber-optic ammonia gas sensors were fabricated via layer-by-layer deposition of poly(diallyldimethylammonium chloride) (PDDA) and tetrakis(4-sulfophenyl)porphine (TSPP) onto the surface of the core of a hard-clad multimode fibre that was stripped of its polymer cladding. The effects of film thickness, length of sensing area, and depth of evanescent wave penetration were investigated to clearly understand the sensor performance. The sensitivity of the fiber-optic sensor to ammonia was linear in the concentration range of 0.5–50 ppm and the response and recovery times were less than 3 min, with a limit of detection of 0.5 ppm, when a ten-cycle PDDA/TSPP film was assembled on the surface of the core along a 1 cm-long stripped section of the fiber. The sensor's response towards ammonia was also checked under different relative humidity conditions and a simple statistical data treatment approach, principal component analysis, demonstrated the feasibility of ammonia sensing in environmental relative humidity ranging from dry 7% to highly saturated 80%. Penetration depths of the evanescent wave for the optimal sensor configuration were estimated to be 30 and

Published by Elsevier. This is the Author Accepted Manuscript issued with:
Creative Commons Attribution Non-Commercial No Derivatives License (CC:BY:NC:ND 4.0).
The final published version (version of record) is available online at DOI:10.1016/j.optlastec.2017.10.027
Please refer to any applicable publisher terms of use.

33 nm at wavelengths of 420 and 706 nm, which are in a good agreement with the thickness of the 10-cycle deposited film (ca. 30 nm).

Keywords: optical fiber; evanescent wave; tetrakis(4-sulfophenyl)porphine; layer-by-layer deposition; *J*-aggregation; ammonia

1. Introduction

Fiber-optic sensing techniques have attracted a great deal of attention in a variety of analytical areas such as chemical and biological sensing [1,2], environmental monitoring [3], and medical diagnostics [4]. In general, the capabilities of the sensing platforms are well-understood, and it is the availability of appropriate functional coatings thatis considered to be the key factor in providing the amplification of the sensitivity and selectivity of sensors towards target analytes that is required for the development of efficient fiber-optic sensors. The creation and development of sensitive materials that can be provide measurable perturbation of the optical signals will expand the application area of fiber-optic sensors. The following characteristics are generally required for the fabrication of sensitive and selective fiber-optic sensors [5]: transparent in appropriate spectral ranges, specific optical changes under the influence of chemical species, fast and reversible response, wide dynamic range, easy immobilization and cheap manufacturing.

Various coating techniques, such as dip- and spin-coating [6,7], layer-by-layer (LbL) deposition or electrostatic self-assembly [8], Langmuir-Blodgett deposition [9] and chemical and physical vapour deposition [10,11] have been employed for functionalization of optical fibers. Among these techniques, the LbL technique, which is based on the alternate adsorption of polycations and polyanions onto solid substrates [12–14], has been shown to a powerful surface modification method. This alternate deposition technique is still expanding its potential because of its

versatility and convenience for the fabrication of nanoassembled thin layers employing various organic and inorganic materials.

Ammonia is one of the major metabolic compounds and the importance of its sensitive detection has been emphasized recently because of its correlation with specific diseases [15–22]. At normal physiological conditions, ammonia can be expelled from the slightly alkaline blood and emanated through the skin or exhaled with the breath. Dysfunction in the kidney or liver that converts ammonia to urea can result in the increase of the ammonia concentration in breath or urine. Consequently, the detection of the ammonia present in breath or urine can be used for the early diagnostics of liver or stomach diseases [16]. The development of sensor devices for measuring ammonia with a sensitivity of 50–2000 ppb and with a fast response time is highly desired [15].

Conventional methods for ammonia detection are based mainly on gas chromatography–mass spectrometry (GC–MS) [16], which, despite its high selectivity and sensitivity, is expensive and time-consuming and requires a well-trained operator. In particular, it is known that real sample measurements must be conducted at high relative humidity (RH) levels (> 90%) [15]. Cheap, small, sensitive, and reliable sensor devices that can efficiently operate at different RH levels could facilitate the creation of point-of-care medical systems that could be used in daily life.

In this regard, optical fibre sensors provide an excellent platform for the development of low cost, small sensitive and reliable ammonia sensors. In the past decades various fibre optic sensing platforms utilising different sensitive layers have been used to develop ammonia sensors. The first-reported fibre optic ammonia sensor, proposed by Wolfbeis, employed the measurement of fluorescence from a pH indicator solution [23]. Since then, a range of optical fibre-based ammonia sensors have been reported, including lossy mode resonances [24], evanescent wave spectroscopy [25, 26, 27], end-reflection, where the sensing

element is at the tip of the fibre, [28, 29] and in-fibre gratings [30]. Generally, the sensitivity of these devices ranged from 10s to 100s of ppm. Table 1 summarizes the parameters of a selection of the ammonia sensors reported in the literature.Table 1: Summary of the ammonia sensor parameters.

Sensor type	Sensitive element	Lower detection limit (LoD)/lowest measured concentration (LMC)	Response time	Reference
Evanescent wave	Universal pH indicator	10ppm(LMC)	5 min	[25]
	bromocresol purple/ bromocresol green, dip coating sol-gel	9ppm (LMC) 0.014 dB/ppm	8 sec	[27]
	bromocresol purple, sol-gel	145 ppm (LMC)	10 sec	[26]
Reflection type	ZrO_2/PSS Nano-assembled	1wt% (LMC)	minutes	[29]
	Oxazine 170 perchlorate	200 ppm (LMC)	-	[28]
Lossy mode resonance	titanium dioxide containing TMPyP	0.1 ppm (LMC)	30 sec	[24]
Grating based	PDDA/TSPP	0.67 ppm (LoD)	-	[30]

In our previous work, we have demonstrated an intrinsic fiber-optic gas sensor with an alternate film of poly(diallyldimethylammonium chloride) (PDDA) and tetrakis(4-sulfophenyl)porphine (TSPP) [31]. The exposure of the nanoassembled film to ammonia induced unique optical changes in the transmission spectrum of the optical fiber, reflecting the characteristic absorption bands (Soret and Q bands) of the assembled TSPP compound.

In this study, the influence on sensor performance of film thickness, the length of sensing area and the penetration depth of evanescent wave are examined in more detail. In addition, the effects of RH, one of the major interference factors in real-life measurements, was thoroughly studied. The sensor's response to ammonia of various concentrations was measured at different RH levels and the results have been statistically analysed via principal component analysis (PCA).

2. Experimental

2.1 Materials

TSPP (*M*w: 934.99) and sodium hydroxide (NaOH) were purchased from Tokyo Kasei (Tokyo, Japan). PDDA (*M*w: 200000–350000, 20 wt% in H_2O) was purchased from Sigma–Aldrich (St. Louis, USA). The TSPP and PDDA chemical structures are shown in Fig. 1. A HCS200 multimode optical fiber, with a silica core and a plastic cladding of diameters 200 μm and 400 μm, respectively, was purchased from Ocean Optics (Largo, USA). Standard ammonia gas of concentration 100 ppm in dry air was purchased in cylinder from Japan Air Gases (Kitakyushu, Japan). Pyridine and toluene, used as additional analyte gases, were purchased from Wako Pure Chemical Industries (Osaka, Japan). All of these chemicals were of analytical grade, and they were used without further purification. Deionized pure water (18.3 MΩ·cm) was obtained by reverse osmosis followed by ion exchange and filtration using a Direct-QTM (EMD Millipore, Billerica, USA).

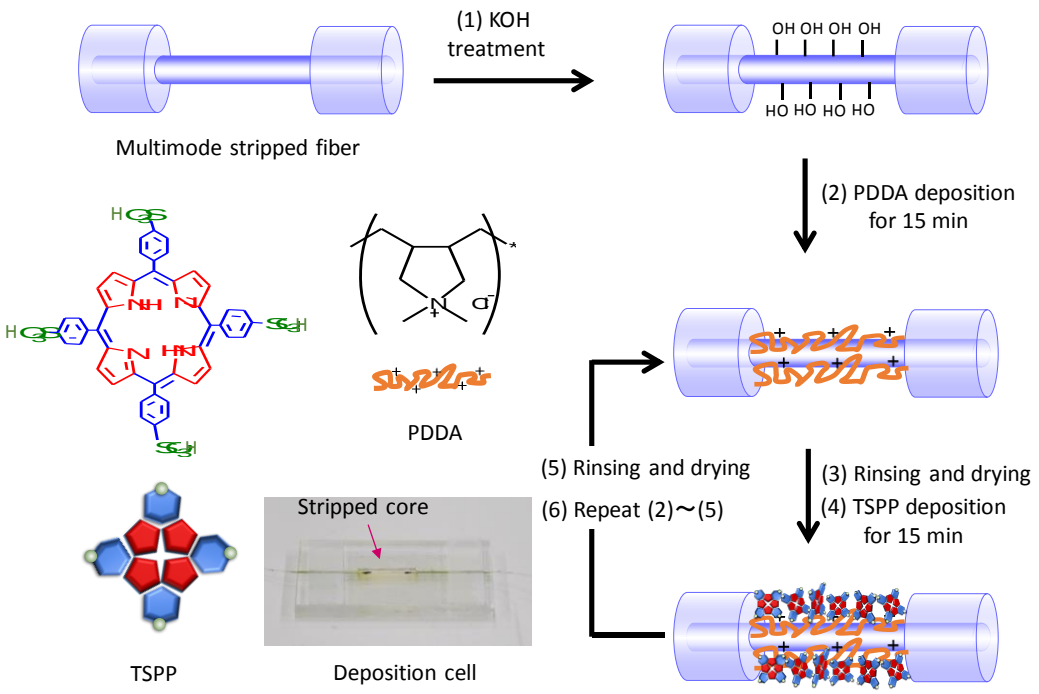

Fig. 1. Chemical structures of TSPP and PDDA and a schematic of the LbL deposition of TSPP and PDDA on a multimode optical fibre.

2.2 Optical fiber preparation

The details of the electrostatic LbL technique employed for the deposition of a porphyrin nanoassembled thin-film onto an optical fiber are described elsewhere [30,31]. Briefly, prior to film deposition, a short section of the plastic cladding was burned off the fiber. The exposed section of the silica core was rinsed in ethanol and deionized water for several times and treated with 1 wt% of ethanolic KOH (ethanol/water = 3 : 2, v/v) for 20 min to functionalize the surface of the silica core with OH groups. The fiber core was then rinsed with deionized water and dried by flushing with nitrogen gas. Thin-films were prepared by alternately immersing the fibre PDDA (0.5 wt% in water, pH 7.8) and TSPP (1 mM in water, pH 4.6) for 15 min each, thereby producing a PDDA/TSPP bilayer. This was achieved by introducing a coating solution (volume 150 ◎L) into a deposition cell with intermediate processes of water washing and drying by flushing with nitrogen gas being undertaken, as illustrated in Fig. 1. The resulting film is denoted by $(PDDA/TSPP)_x$, where x

indicates the number of deposition cycles. To check the effect of the film thickness, 5-, 10-, and 15-cycle films were deposited on the activated core of the optical fiber and in every case the outermost surface of the alternate film was TSPP.

One end of the optical fiber was connected to a deuterium-halogen light source (DH-2000-Ball, Mikropack), while the other end was connected to a spectrometer (S1024DW, Ocean Optics) to monitor the assembly process. The absorbance was determined by taking the logarithm of the ratio of the transmission spectrum of the coated fiber, $T(\lambda)$, to the transmission spectrum measured prior to film deposition $T_0(\lambda)$.

$$A(\lambda) = -\log [T(\lambda) / T_0(\lambda)], \quad (1)$$

2.3 Optical measurement set-up

Desired gas concentrations were produced using a two-arm flow system, as shown in Fig. 2. A specially designed Teflon chamber was used to allow the sensor to be exposed to varying analyte concentrations [31]. The stripped section of the optical fiber, coated with the functional film, was inserted inside the chamber and connected to the light source and spectrometer. The final ammonia concentration (volume fraction) c in the measurement chamber was calculated using the following formula:

$$c \text{ (ppm)} = (L_1 \cdot z) / (L_1 + L_2), \quad (2)$$

where z is the original concentration of ammonia in cylinder, and L_1 and L_2 are the flow rates of the dry air and ammonia gas, respectively. L (where $L = L_1 + L_2$) was kept constant at 1 L/min and the final ammonia concentration was adjusted by varying L_1 and L_2.

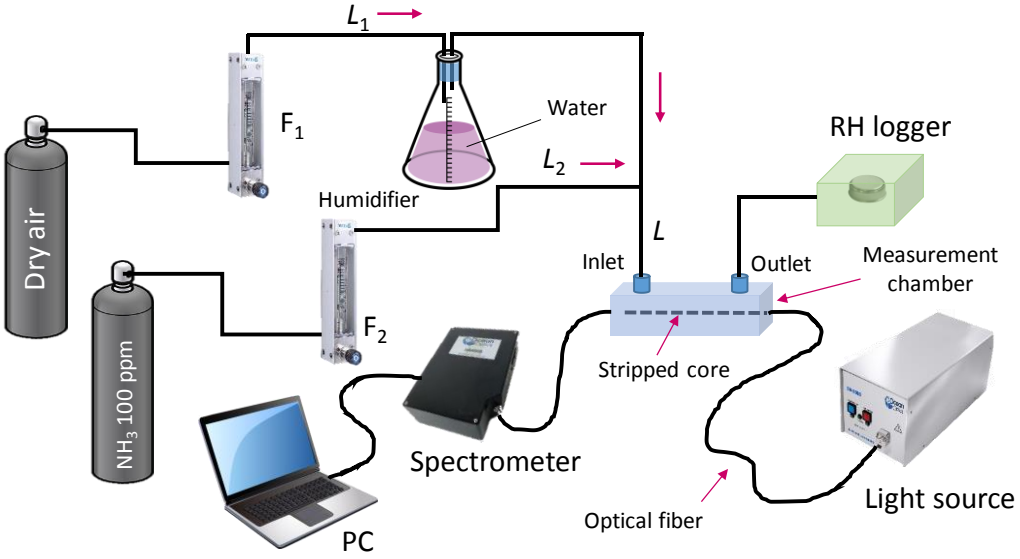

Fig. 2. Apparatus of a two-arm flow gas generation system and schematic of the measurement setup. F_1 and F_2 are flowmeters; L_1 and L_2 are flow rates of dry air and ammonia gas.

For ammonia measurements at different RH levels, the dry compressed air was passed through a humidifier, as shown in Fig. 2. Different RH levels were obtained by varying the depth of the tube in the humidifier. A humidity logger (Hygrochron, KN Laboratories: RH range of 0–95%; accuracy ±5% at 25 °C in the range of 20–80% RH and reading resolution 0.1%) was used to measure the humidity inside the measurement chamber. The baseline spectrum of each experiment was recorded by passing dry air through the measurement chamber until the signals measured at the wavelengths of 470 and 706 nm reached equilibrium. The optical sensor response, *SR*, was calculated using the following equation:

$$SR\ (\%) = 100\ (I_0 - I)\ /\ I_0, \tag{3}$$

where I_0 and I describe the light intensity of the TSPP film in the absence and presence of an analyte gas, respectively, measured at the same wavelength (at or near peaks of the difference spectrum).

3. Results and Discussion

3.1 Optimization of coating parameters

As demonstrated in our previous work, TSPP has two distinct types of aggregates (*J*- and *H*-), together with monomers in the nano-assembled film. The relative abundances of these structures change as the degree to which the TSPP is protonated or deprotonated changes [32–35]. The assembly of the PDDA and TSPP layers after each deposition cycle was measured by monitoring optical changes in the transmission spectra of the optical fiber. The transmission spectra of the optical fiber recorded during the deposition of a 15-cycle PDDA/TSPP thin film are shown in Fig. 3a and b when the outermost layer was PDDA and TSPP, respectively. Fig. 3c shows intensity changes in the transmission spectra of the 15-cycle PDDA/TSPP film with an outermost layer of TSPP, which were monitored at wavelengths 420, 470, 490, 706 nm, versus the number of deposition cycles. It is confirmed that after ten deposition cycles, all transmission peaks become less pronounced and further deposition does not bring significant changes in the intensity. In particular, when the length of the stripped silica core was increased to of 3 cm, this phenomenon becomes more apparent (Fig. S1), which may be a result of the longer interaction length between the evanescent wave and the PDDA/TSPP film. The 3 cm-striped optical fiber shows faster saturation in absorbance as compared with the 1 cm-striped one, which is attributed to the characteristics of evanescent wave spectroscopy which is the measurement principle upon which the operation of the sensor is based. The intensity of the evanescent wave decays exponentially with the increase of the distance from the surface of the fiber core. In addition, the strong absorption of light by the TSSP in the sensor film is a significant factor in decreasing the effective penetration depth of the evanescent wave.

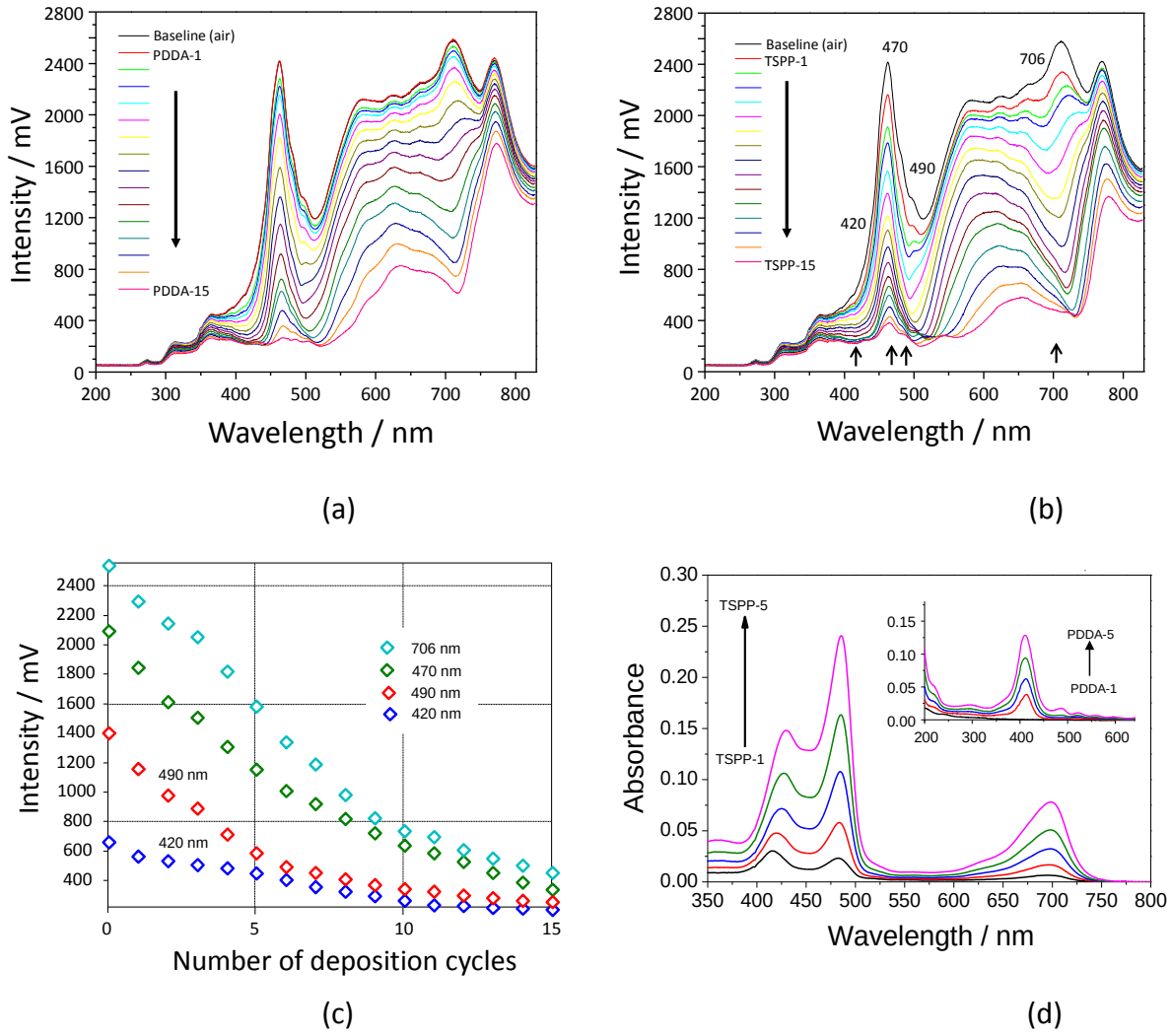

Fig. 3. Evolution of transmission spectra of the PDDA/TSPP alternate layers deposited onto the 1 cm-stripped core of the fiber when the outermost layer was (a) PDDA and (b) TSPP. (c) Intensity changes in the transmission spectra in (b), which were measured at 420, 470, 490, 706 nm. (d) UV–vis absorption spectra of a 5-cycle PDDA/TSPP alternate film prepared on a quartz plate when the outermost layer was TSPP. The insert of (d) shows UV–vis absorption spectra of the same film when the outermost layer was PDDA.

Most plausibly the changes in the transmission spectra of the optical fiber shown in figure 3 are related to the TSPP aggregation structures in the film and their corresponding optical properties. To examine this in more detail, the UV–vis absorption spectra of the alternate PDDA and TSPP layers deposited on a quartz plate were used to characterize the TSPP assemblies in the film. The evolution of the UV–vis absorption spectra during the deposition of a PDDA/TSPP thin film onto a quartz plate over five deposition cycles is shown in Fig. 3d. The absorption spectra

for the individual layers with an outermost layer of TSPP were characterized by a double peak in the Soret band at 429 and 485 nm and by a pronounced Q band peak at around 700 nm. However, when the film had an outermost layer of PDDA there was a single peak in the Soret band at 410 nm (inset of Fig. 3d).

In general, the aggregation state of TSPP and its spectral features are controlled by the protonation/deprotonation of the porphyrin pyrrole ring [32–35]. It is well known that the specific Soret bands of TSPP can be identified by four different arrangements; free-base, *H*-aggregate, diacid, and *J*-aggregate with corresponding absorption bands centres at 413, 423, 434, and 491 nm, respectively [36–40]. Therefore, the spectral features of the film at 429, 485, and 700 nm, which are red-shifted compared with those in the monomeric free-base and diacid states, suggest that the TSPP molecules in the film are preferentially present in the *J*-aggregate state along with a small amount of *H*-aggregates.

3.2 Penetration depth calculation

The penetration depth for the given measurement set-up was calculated to check the optimal thickness of the sensitive layer. As the number of the PDDA and TSPP layers increases the absorbance reaches saturation. However, a linear increase of the absorbance is observed when the essentially same PDDA/TSPP film is assembled on a quartz substrate to a thickness of 15 bilayers [32, 41]. This difference between the films deposited onto the quartz substrate and the optical fiber could be related to the penetration depth of the evanescent wave, which is changed significantly when absorbing films are deposited on the optical fiber.

To calculate the effect of the film optical thickness on the sensor performance, the penetration depth of the evanescent wave was estimated. For this purpose, the absorbance of the film was taken into account. The evanescent wave is an electric field that extends from the surface of the fiber core into the lower index surrounding medium and decays exponentially with distance from the surface, generally over a distance from hundred to several hundred nanometres. For

multimode waveguides, the penetration depth d_p is defined as the distance from the surface at which the strength of the evanescent wave decays for 1/e of its value and is approximately given by:

$$d_p(\lambda,\theta)=\lambda / (2\pi [n_c^2\sin^2\theta - n_{sm}^2]^{1/2}), \quad (4)$$

where n_c and n_{sm} are refractive indices of the optical fiber and surrounding medium, respectively, and θ is the angle of incidence. In our case, the thin film deposited on fiber core is a strongly absorbing material and the imaginary component of n_{sm} should be taken into account [42]. The intensity of the evanescent wave can be written as (5):

$$I(\lambda,\theta) = I_0 e^{-\left(\frac{1}{d_p(\lambda,\theta)}+\varepsilon(\lambda)\right)x}, \quad (5)$$

where I is the intensity of the wave at a distance x from the surface of the core, I_0 is the intensity at the core surface and ε is an absolute extinction coefficient of the deposited film. The penetration wave in this case will be given by (6):

$$d_{AAP}(\lambda,\theta) = \frac{1}{\frac{1}{d_p(\lambda,\theta)}+\varepsilon(\theta)} = \frac{d_p(\lambda,\theta)}{1+d_p(\lambda,\theta)\varepsilon(\lambda)}, \quad (6)$$

where the absolute extinction coefficient $\varepsilon(\lambda)$ is obtained from the absorption spectra of the PDDA/TSPP film (Fig. 3d) and the film thickness d_f = 30 nm [32].

The dependence of the penetration depth on wavelength is shown in Fig. 4a, which was determined using the following parameters: n_c = 1.48 and n_f = 1.42 [43] for the refractive indices of the core and deposited film, respectively; θ = 90º, which was chosen since at this value the penetration depth for the light propagating along the multimode fiber is minimal; and $\varepsilon(\lambda)$ extinction coefficient, which was calculated from the experimentally measured absorption spectrum of the $(PDDA/TSPP)_{10}$ film deposited onto the quartz slide.

Fig. 4b shows the dependence of the evanescent wave attenuation upon the distance from the core interface for the 1- and 10-cycle PDDA/TSPP films. The penetration depths at 420 and 706 nm are estimated to be 34 and 50 nm for the

1-cycle film and 30 and 33 nm for the 10-cycle film, respectively. Based on these calculations, we can conclude that optimal film thickness in our case was ca. 30 nm and this thickness induced optimal interaction with the evanescent wave.

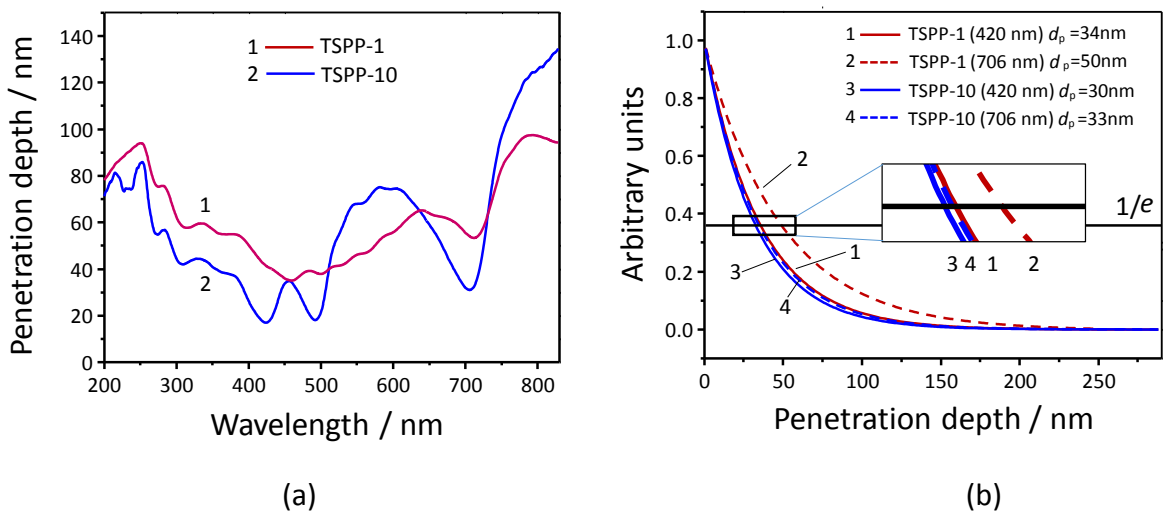

Fig. 4. (a) Dependence of the penetration depth of the evanescent wave on wavelength and (b) decay of the evanescent wave calculated at 420 and 706 nm for the 1-and 10-cycle PDDA/TSPP films.

3.3 Optical response to ammonia

Spectral changes (obtained by subtracting a transmission spectrum measured at a given ammonia concentration from that measured in air) induced by the presence of ammonia on the 10-cycle PDDA/TSPP film are shown in Fig. 5a. Similar to the previously reported 5-cycle PDDA/TSPP film [31], as the ammonia concentration increased from 0 ppm up to 40 ppm, the intensity of the obtained spectra increased at 706 nm, while at 250–400 nm, 470 nm and 658 nm it decreased. These spectral changes in the transmission spectra can be ascribed to the distortion of the *J*-aggregates of TSPP upon the adsorption of the ammonia gas. In particular, the spectral characteristics at 470 and 658 nm suggest that the TSPP molecules in the *J*-aggregation state are returned to the protonated mono- and di-acidic forms due to the film exposure to ammonia. Upon exposure of the $(PDDA/TSPP)_{10}$ film to ammonia, the most noticeable change in intensity was observed at 706 nm. Moreover, as predicted from the above penetration depth calculations, the 10-cycle

film provided higher response to ammonia in comparison with the 5- and 15-cycle films, as shown in Fig. 5b.

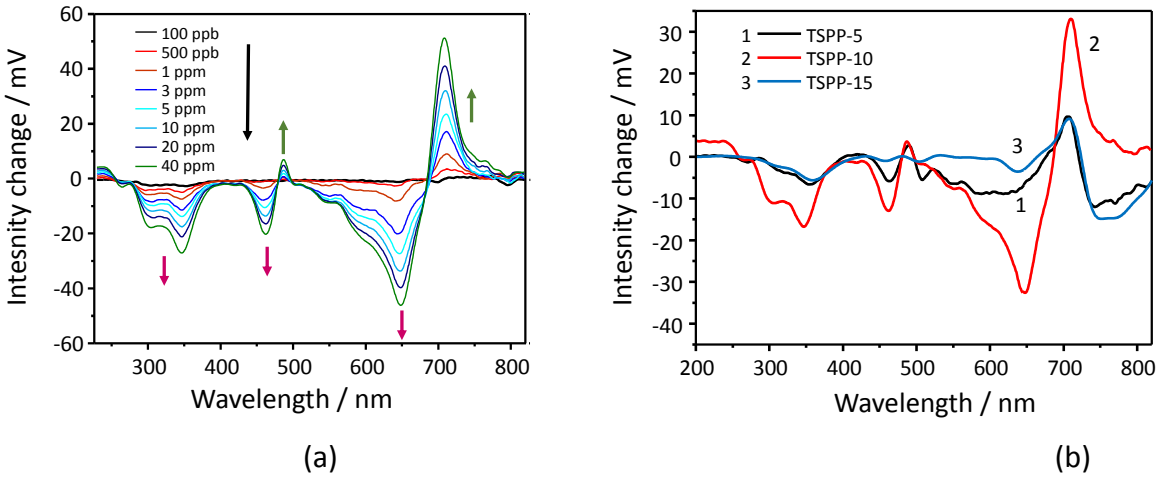

Fig. 5. (a) Evolution of the difference transmission spectra induced by the exposure of the optical fiber modified with a $(PDDA/TSPP)_{10}$ film to ammonia of concentrations ranging from 100 ppb to 40 ppm. (b) Comparison of the difference transmission spectra at 10 ppm ammonia for the 5-, 10-, and 15-cycle PDDA/TSPP films.

The response and recovery times of the fiber sensors are summarized in Table 1. In the case of the $(PDDA/TSPP)_{10}$ film, the values are within 2.1 min and 3.9 min, respectively (Fig. 6a, Table 1). The calibration curves were plotted from the recorded spectra at given ammonia concentrations. The fiber sensors show linear responses to ammonia with sensitivities of 0.50 ± 0.07, 1.70 ± 0.28, and 0.90 ± 0.09%/ppm for the 5-, 10-, and 15-cycle PDDA/TSPP films, respectively (Fig. 6b). The corresponding limits of detection (LODs), defined using a 3σ method (Fig. 6b), were estimated to be 3.0, 0.4 and 1.4 ppm for 5-, 10-, and 15-cycle PDDA/TSPP films, respectively (Table 1).

The sensitivity appears to depend on the thickness of the coating; the 10-cycle film exhibits the highest sensitivity to ammonia, while the 5- and 15-cycle films have lower values. This can be attributed to the higher concentration of TSPP in the 10-cycle film as compared to the 5-cycle film and hence larger numbers of reaction sites for ammonia adsorption are available. On the other hand, the lower sensitivity

of the 15-cycle film, in spite of the higher amount of TSPP present inside the film as compared to the 10-cycle film, most plausibly is due to the inefficient interaction between the evanescent wave and the sensitive layer. These results are in a good agreement with the penetration depth calculation (Fig. 4a and b), from which the efficient interaction between the evanescent wave and the 10-cycle PDDA/TSPP film was found to be ca. 30 nm.

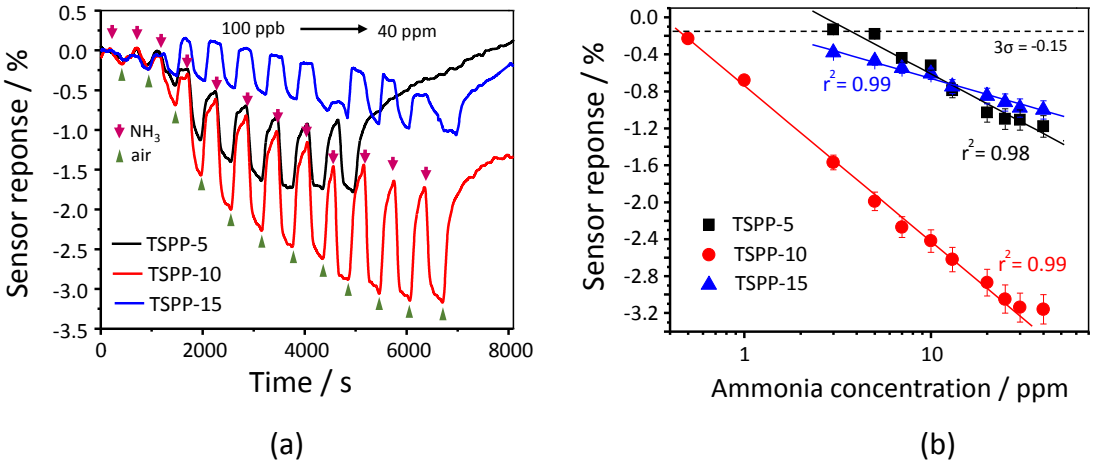

Fig. 6. (a) Dynamic sensor responses (calculated using Eq. 3) at 706 nm and (b) calibration curves plotted using data measured at 706 nm for the 5-, 10-, and 15-cycle PDDA/TSPP films.

Table 1. Sensing parameters of the PDDA/TSPP films with different deposition layers.

Sample name	Thickness, nm	Sensitivity, slope [a], %/ppm	Response time [b], min	Recovery time [b], min	Linear range, ppm	*LOD* [c], ppm
$(PDDA/TSPP)_5$	15	0.50 ± 0.07	1.6	3.2	0.5–40	3.0
$(PDDA/TSPP)_{10}$	30	1.60 ± 0.28	2.1	3.9	0.5–40	0.4
$(PDDA/TSPP)_{15}$	45	0.90 ± 0.09	4.7	1.2	0.5–40	1.4

[a] Slope calculated from the calibration curve (Fig. 6b, at 706 nm).
[b] Determined as an interval needed for the signal to achieve 90% of its saturated condition when measured for ammonia at a concentration of 10 ppm..
[d] Defined using a 3σ method, where σ is the standard deviation (0.05).

Therefore, an excessive increase in the film thickness will cause inefficient interaction between the evanescent wave and the TSPP molecules. Interestingly, this problem is not observed when the same films were assembled on quartz substrates [32, 41]. The highest sensitivity was observed in the 15-cycle film, which

is related to the higher amount of the binding sites present in the thicker film. Nevertheless, the sensitivity of the fiber-optic sensor modified with a 10-cycle PDDA/TSPP film is ca. 20 times higher than that of the 15-cycle PDDA/TSPP film deposited on the quartz substrate [32], which is a result of the characteristics of the evanescent wave fiber-optic sensor.

3.4 Influence of humidity on the sensor response

For practical application of the prepared fiber sensors, RH is one of the most important interfering parameters, and thus the influence of RH on the sensor performance was investigated. Fig. 7a shows RH–induced difference spectra of the $(PDDA/TSPP)_{10}$ film-coated optical fiber, which were obtained by subtracting the transmission spectrum measured at 7% RH (dry air) from the transmission spectra measured at different RH levels (20%, 30%, 50%, 70%, and 80%). In contrast to the response to ammonia, when the RH was changed the transmission of the fiber sensor was influenced over the entire spectral range. These optical changes in the transmission spectra may be attributed to the increased light scattering when a certain amount of water vapor is adsorbed on the sensitive coating. In addition, the assembled PDDA and TSPP film can swell as the humidity increases, leading to an increase of the optical thickness, which results in a decrease in the intensity in the transmission spectrum.

It should be noted that the baseline used for the intensity difference calculation was the transmission spectrum obtained at 7% RH. The dynamic change in the intensity measured at 706 nm is shown in Fig. 7b, where the carrier gas was changed from dry air (7% RH) to the humidified air with RH values of 20%, 30%, 50%, 70%, and 80%. The intensity decreased rapidly in a wide spectral range when the RH was changed from 7% to 20% and from 20% to 30%; however, the response to humidity is almost saturated at a RH over 30% RH, indicating the stability of the optical parameters of the device in the wide range of RH between 30%–80%. The initial intensity decrease observed for RH in the range 7% to 30% may be attributed

to structural changes (e.g., film swelling, TSPP aggregation) in the film. Usually, indoor humidity levels are maintained in the RH range from 30% to 80%. This therefore allows the current fiber sensor to be utilized in real environments.

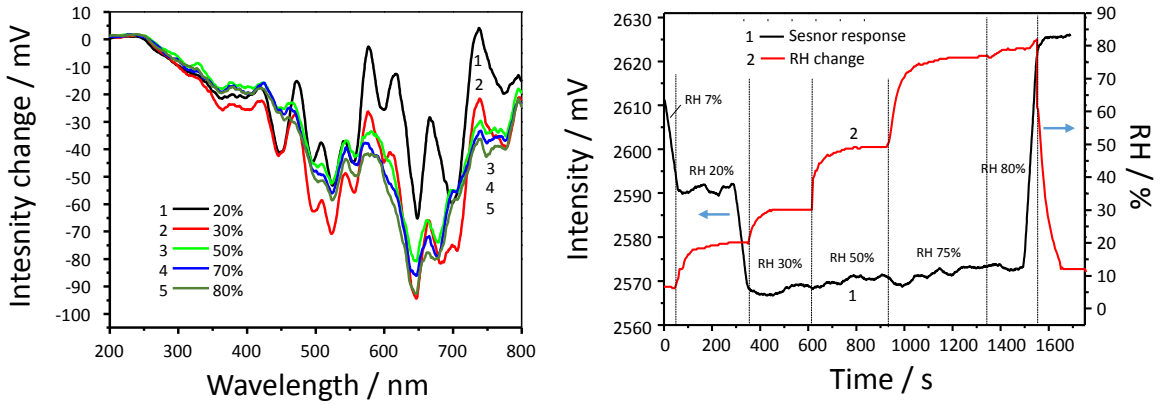

Fig. 7. (a) Difference spectra of the 10-cycle PDDA/TSPP film, obtained by subtracting the transmission spectrum measured at 7% RH (dry air) from the transmission spectra measured at different RH levels (20, 30, 50, 70 and 80%). (b) Dynamic sensor response at 706 nm measured at different humidity levels that were measured using a humidity data logger.

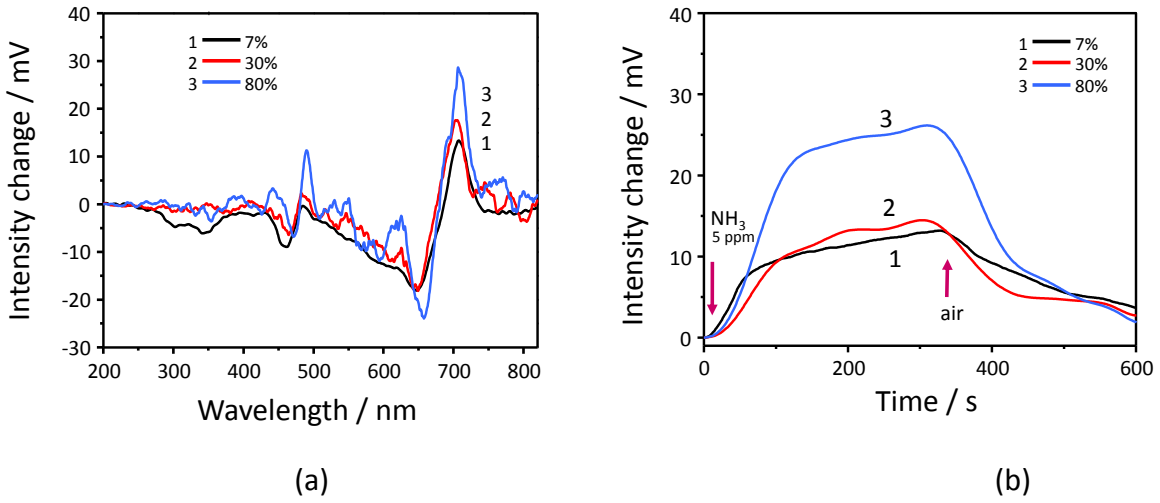

Fig. 8. (a) Comparison of the difference transmission spectra of the 10-cycle PDDA/TSPP film in the presence of 5 ppm ammonia and (b) dynamic sensor responses at 706 nm to 10 ppm ammonia at different RH levels (7, 30, and 80%).

The data logger and optical fibre sensor were not synchronised to the same clock, which caused the small delay between the measurements (less than 2-3 sec) in Figure 7(b).

The sensor's response to humidity was 0.006%/rH% in the range of humidity from 30 to 80%, 0.08%/ rH% when humidity changed from 10 to 20% and 0.03% when humidity changed from 80 to 10%.Figure 7(b).

The influence of RH on the sensitivity to ammonia is shown in Fig. 8. Different spectral features were observed when the $(PDDA/TSPP)_{10}$ film was exposed to 5 ppm ammonia at different RH levels, as shown in Fig. 8. An increase in RH led to an increase in the ammonia-induced intensity change at 706 nm along with a diminishing intensity change at shorter wavelengths (Fig. 8a). Most plausibly, the increase of the sensitivity to ammonia at higher humidity levels is a result of the increased solubility of ammonia into the film.

The stability of the sensor response was tested by repeated short-time (< 30 s) exposure of the $(PDDA/TSPP)_{10}$ film to 30 ppm ammonia (Fig. 9a). A similar study had shown that short-time exposure to the analyte gas results in high stability and fast recovery of the sensor response [44]. The sensor response to even relatively high ammonia concentration (30 ppm) was fully reversible and repeatable over the whole spectral range, which could be achieved by flushing the $(PDDA/TSPP)_{10}$ film with pure air; however, the observed intensity change, ca. 10 mV, was lower when compared with the response obtained by longer time exposure of the film at the same concentration of ammonia (ca. 40 mV).

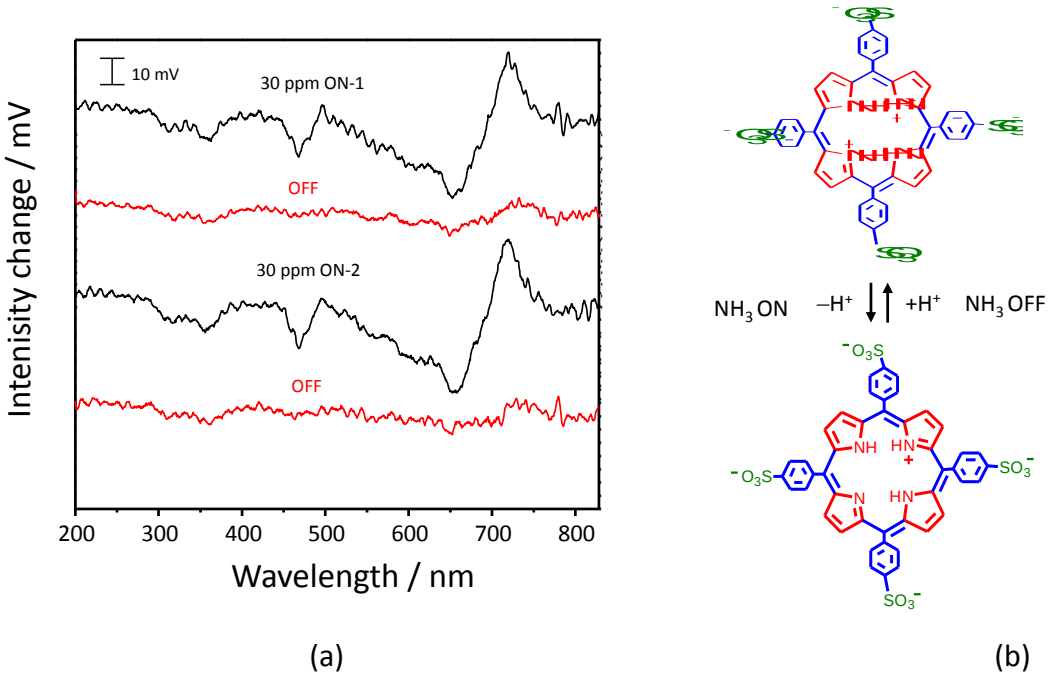

Fig. 9. (a) Difference spectra obtained by short time exposure (< 30 s) of the 10-cycle PDDA/TSPP film to 30 ppm ammonia (black lines) and their recovery by flushing dry air at 7% RH (red lines). (b) Schematic of the mechanism based on the ammonia-induced deprotonation of TSPP.

Th fast and reversible response and recovery of the PDDA/TSPP alternate film-modified fiber sensors can be explained by the structural reversibility of the *J*-aggregates of TSPP. Initially, most of the TSPP molecules are present in the *J*-aggregation state in the film. Exposure of the film to the ammonia gas will lead to the deprotonation of the TSPP molecules. Consequently, this distorts and dilutes the *J*-aggregates, eventually being returned to the monomeric state when the concentration of ammonia is very high (e.g. over 500 ppm) [31]. However, the TSPP molecules in the *J*-aggregate state can be changed from the di-acidic form to mono-acidic form by ammonia-induced deprotonation at concentrations of ammonia less than 100 ppm, as schematically shown in Fig. 9b. This structural change of the TSPP is clearly confirmed from the spectral features at 470, 658, and 706 nm in Fig. 9a. Therefore, we can conclude that the current fiber sensor system enables a detailed analysis of the mechanism of ammonia gas sensing.

3.6 PCA analysis

As was demonstrated above, the 10-cycle PDDA/TSPP film-modified fiber-optic sensor is sensitive to both humidity and ammonia and it is not a trivial task to discriminate the influence of humidity on the sensor response to ammonia. For the purpose of qualitative data description, the obtained results were analyzed using a simple statistical data treatment approach, PCA (Statistical EXCEL add-in, V. 5.05 by Esumi Co. Ltd.) by reducing the multi-dimensionality of the obtained data. The sensor response measured at four wavelengths (356, 470, 658, and 706 nm), at which the biggest intensity changes were observed, were manually chosen as PCA variables from the difference spectra induced by both humidity and ammonia. These selections were sufficient to obtain good separation between qualitatively different samples. The PCA results are shown in Fig. 10a, with a 96.5% cumulative proportion of PC1 and PC2. As can be noted, the largest part of data is reduced to the first principal component, PC1 (74.4%), while the second principal component, PC2 (22.1%), comprises a lower amount of information of the total variability. From the loading plot (Fig. 10b), we can conclude that two wavelengths at 470 and 706 nm contribute significantly to the determination of the ammonia concentration at higher humidity levels.

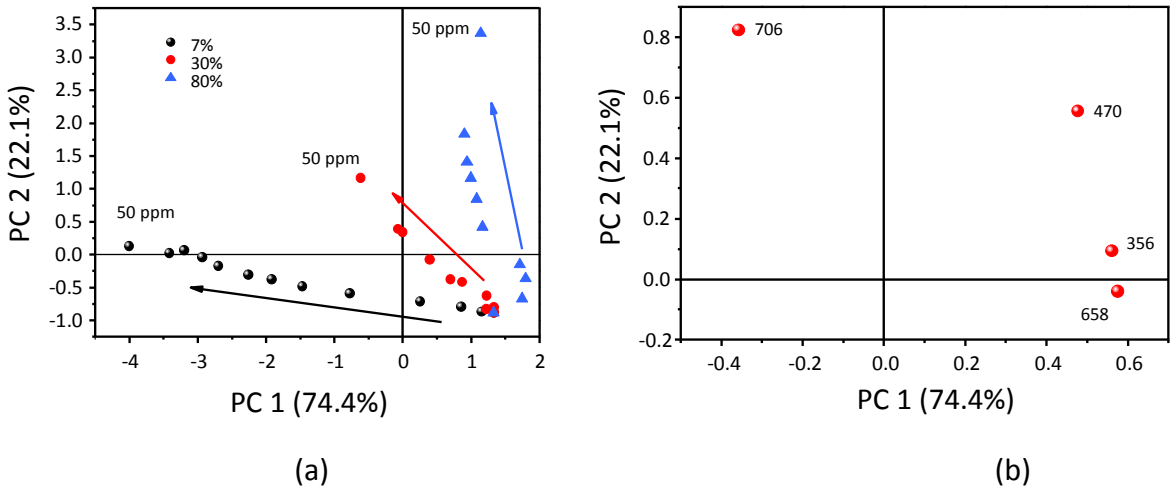

Fig. 10. (a) Principal component analysis performed using data measured in the presence of ammonia of concentrations ranging from 100 ppb to 40 ppm at different RH levels (7%, 30%, and 80%). (b) PCA loadings of the four selected wavelengths at 356, 470, 658, and 706 nm.

In addition, different analytes (toluene and pyridine) were tested to confirm the selectivity of the sensor. There was no measurable change in the optical transmission spectrum when the $(PDDA/TSPP)_{10}$ film was exposed to toluene and pyridine (100 ppm each, data not shown), indicating the high selectivity of the sensor's response to ammonia.

4. Conclusions

Parameters for fiber-optic chemical sensor development were investigated and optimized for sensitive and selective ammonia gas detection. The optimal sensor performance was achieved with a 10-cycle (PDDA/TSPP)-coated optical fiber with a film thickness of ca. 30 nm that is in a good agreement with the estimated penetration depth of the evanescent wave for the given sensor configuration. The 10-cycle deposited sensor showed a linear sensitivity in the presence of ammonia with a limit of detection of 0.4 ppm in the concentration range of 0.5–50 ppm and its response/recovery times were less than 3 min under optimal conditions. The optical parameters of the device were stable in the wide range of RH between 30%–80%. Moreover, the sensitivity towards ammonia could be improved at higher RH levels, which suggests that the current fiber sensor can be used in the real environments.

The demonstrated sensor offers an opportunity for the detection of ammonia in breath at high humidity levels. Furthermore, the current study provides a methodology for sensor architecture that is capable of expanding the range of analytes to be detected by using different types of coating materials. Our future work will be focused on improvement of the current sensor system to selectively discriminate ammonia and other chemicals co-present in human breath, which would be of importance in non-invasive medical diagnosis.

Acknowledgments

This work was supported by MEXT via 2nd Kitakyush Knowledge-based Cluster Project (Regional Innovation Cluster Program (Global Type). S.-W. Lee also acknowledges the grant-in-aid for scientific research (A) (15H01713) from the Japan Society for the Promotion of Science.

Appendix A. Supplementary data

Supplementary data associated with this article can be found, in the online version, at https://doi.org/10.1016/j.optlastec.2017.10.027.

References

1. S. Korposh, S.W. James, S.-W. Lee, S.M. Topliss, S.C. Cheung, W.J. Batty, and R.P. Tatam, Fiber optic long period grating sensors with a nanoassembled mesoporous film of SiO_2 NPs, *Opt. Express* **18**, 13227–13238 (2010).
2. J. Zhang, X. Tang, J. Dong, T. Wei, and H. Xiao, Zeolite thin film-coated long period fiber grating sensor for measuring trace organic vapors, *Sens. Act. B* **135**, 420–425 (2009).
3. C.K. Ho, A. Robinson, D.R. Miller, and M.J. Davis, Overview of sensors and needs for environmental monitoring, *Sensors* **5**, 4–37(2005).
4. C.D. Natale, A. Macagnano, E. Martinelli, R. Paolesse, G. D'Arcangelo, C. Roscioni, A. Finazzi-Agrò, and A. D'Amico, Lung cancer identification by the analysis of breath by means of an array of non-selective gas sensors, *Biosens. Bioelectron*. **18**, 1209–1218 (2003).
5. K.T.V. Grattan and B.T. Meggitt, Chemical and environmental sensing, Boston: Kluwer Academic Publisher (1999).
6. G. Queroa, A. Crescitelli, D. Paladino, M. Consales, A. Buosciolob, M. Giordano, A. Cutolo, and A. Cusano, Evanescent wave long-period fiber grating within D-shaped optical fibers for high sensitivity refractive index detection, *Sens. Act. B* **152**, 196–205 (2011).
7. M. Shadaram, L. Espada, J. Martinez, and F. Garcia, Modeling and performance evaluation of ferrocene-based polymer clad tapered optical fiber gas sensors, *Opt. Eng.* **37**, 1124–1129 (1998).
8. J.M. Corres, F.J. Arregui, and I.R. Matias, Sensitivity optimization of tapered optical fiber humidity sensors by means of tuning the thickness of nanostructured sensitive coatings, *Sens. Act. B* **122**, 442–449 (2007).
9. S.W. James and R.P. Tatam, Fibre optic sensors with nano-structured coatings, *Journal of Optics A: Pure and Applied Optics* **8**(7), S430–S444 (2006).
10. Y.-C. Tsao, Y.-C. Lin, W.-H. Tsai, and M.-S. Wu, Investigation of optic fiber

sensor based on surface plasmon resonance for monitoring the concentration of plasma deposited hydrophilic functional groups on material surfaces, *Sens. Act. A* **166**, 9–13 (2011).

11. W.B. Lin, M. Lacroix, J.M. Chovelon, N. Jaffrezic-Renault, and H. Gagnaire, Development of a fiber-optic sensor based on surface plasmon resonance on silver film for monitoring aqueous media, *Sens. Act. B* **75**, 203–209 (2001).
12. G. Decher, J.-D. Hong, and J. Schmitt, Buildup of ultrathin multilayer films by a self-assembly process: III. Consecutively alternating adsorption of ionic and cationic polyelectrolytes on charged surfaces, *Thin Solid Films* **210/211**, 831–835 (1992).
13. A.G. Decher and J.D. Hong, Buildup of ultrathin films by a self-assembly process: Consecutive adsorption of anionic and cation bipolar amphiphiles and polyelectrolytes on charged surface, *Ber. Bunsenges. Phys. Chem*. **95**, 1430–1434(1991).
14. J.J. Ramsden, Yu. M. Lvov, and G. Decher, Optical and X-ray structural monitoring of molecular films assembled via alternate polyion adsorption, *Thin solid Films* **254**, 246–251 (1995); **261**, 343–344 (1995).
15. B. Timmer, W. Olthuis, and A. Van den Berg, Ammonia sensors and their applications–a review, *Sens. Act. B* **107**, 666–677 (2005).
16. C. Turner, P. Španěl, and D. Smith, A longitudinal study of ammonia, acetone and propanol in the exhaled breath of 30 subjects using selected ion flow tube mass spectrometry, SIFT-MS, *Physiol. Meas.* **27**, 321–37 (2006).
17. I.D. Weiner, W.E. Mitch, and J.M. Sands, Urea and ammonia metabolism and the control of renal nitrogen excretion, *Clin. J. Am. Soc. Nephrol*. 10311013 (2014).
18. F.M. Schmidt, O. Vaittinen, M. Metsälä, M. Lehto, C. Forsblom, P.H. Groop, and L. Halonen, Ammonia in breath and emitted from skin, *J. Breath Res*. **7**, 017109 (2013).
19. L.R. Narasimhan, W. Goodman, and C.K.N. Patel, Correlation of breath

ammonia with blood urea nitrogen and creatinine during hemodialysis, *Proc. Natl. Acad. Sci. U. S. A*. **98**, 4617–4621 (2001).

20. J.P. Ong, A. Aggarwal, D. Krieger, K.A. Easley, M.T. Karafa, F. Van Lente, A.C. Arroliga, and K.D. Mullen, Correlation between ammonia levels and the severity of hepatic encephalopathy, *Am. J. Med*. **114**, 188–193 (2003).
21. J.G. Kusters, A.H.M. Van Vliet, and E.J. Kuipers, Pathogenesis of Helicobacter pylori infection, *Clin. Microbiol. Rev*. **19**, 449–490 (2006).
22. A. Tangerman and E.G. Winkel, Extra-oral halitosis: an overview, *J. Breath Res*. **4**, 017003 (2010).
23. O. S. Wolfbeis, H. E. Posch, Fibre-optic fluorescing sensor for ammonia, *Analytica Chimica Acta*, **185**, 321-327 (1986).
24. D. Tiwari, K. Mullaney, S. Korposh, S. W. James, S.-W. Lee, R. P. Tatam, An ammonia sensor based on Lossy Mode Resonances on a tapered optical fibre coated with porphyrin-incorporated titanium dioxide, Sensors and Actuators B: Chemical, 242, 645-652, (2017).
25. Rodríguez, Adolfo J. et al. "A Fiber Optic Ammonia Sensor Using a Universal pH Indicator." Sensors (Basel, Switzerland) 14.3, 4060–4073, (2014).
26. W. Cao, Y. Duan, Optical fiber-based evanescent ammonia sensor, Sensors and Actuators B: Chemical, 110(2), 252-259, (2005).
27. T. Yagi, et al., Fiber-optic ammonia sensors utilizing rectangular-cladding eccentric-core fiber. Optical Review,. 4(5): p. 596-600,(1997).
28. C.-S. Chu and Y.-F. Chen, Development of ratiometric optical fiber sensor for ammonia gas detection, in Proc. Of SPIE Vol. 10323, 103231P, (2017).
29. Galbarra, D., et al., Ammonia optical fiber sensor based on self-assembled zirconia thin films. Smart Materials and Structures, 2005. 14(4): p. 739-744.
30. T. Wang, W. Yasukochi, S. Korposh, S.W. James, R.P. Tatam, and S.-W. Lee, A long period grating optical fiber sensor with nano-assembled porphyrin layers for detecting ammonia gas, *Sens. Act. B* **228**, 573–580 (2016).

31. S. Korposh, S. Kodaira, W.J. Batty, S.W. James, and S.-W. Lee, Nano-assembled thin film gas sensor. II. An intrinsic high sensitive fibre optic sensor for ammonia detection, *Sens. Mater.* **21**, 179–189 (2009).
32. S.O. Korposh, N. Takahara, J.J. Ramsden, S-W. Lee, and T. Kunitake, Nano-assembled thin film gas sensors. I. Ammonia detection by a porphyrin-based multilayer film, *J. Biological Physics and Chemistry* **6**, 125–132 (2006).
33. K. Ariga, Y. Lvov, and T. Kunitake, Assembling Alternate Dye−Polyion Molecular Films by Electrostatic Layer-by-Layer Adsorption, *J. Am. Chem. Soc*. **119**, 2224–2231 (1997).
34. P. Gregory van Patten, A.P. Shreve, and R.J. Donohoe, Structural and Photophysical Properties of a Water-Soluble Porphyrin Associated with Polycations in Solution and Electrostatically-Assembled Ultrathin Films, *J. Phys. Chem. B* **104**, 5986–5992 (2000).
35. V. Snitka, M. Rackaitis, and R. Rodaite, Assemblies of $TPPS_4$ porphyrin investigated by TEM, SPM and UV–vis spectroscopy, *Sens. Act. B* **109**, 159–166 (2005).
36. D.L. Akins, H.R. Zhu, and C.J. Guo, Absorption and Raman Scattering by Aggregated meso-Tetrakis(p-sulfonatophenyl)porphine, *Phys. Chem*. **98**, 3612–3618 (1994).
37. J.M. Ribó, J. Crusats, J.-A. Farrera, and M.L. Valero, Aggregation in water solutions of tetrasodium diprotonated meso-tetrakis(4-sulfonatophenyl)porphyrin, *J. Chem. Soc., Chem. Commun*. **6**, 681–682 (1994).
38. R. Lauceri, S. Gurrieri, E. Bellacchio, A. Contino, L. Monsu'scolaro, A. Romeo, A. Toscano, and R. Purrello, J-Type Aggregates of the Anionic Meso-Tetrakis(4-Sulfonatophenyl)Porphine Induced by 'Hindered' Cationic Porphyrins, *Supramol. Chem*. **12**, 193–202 (2000).
39. R. Rotomskis, R. Augulis, and V. Snitka, Hierarchical Structure of TPPS4

J-Aggregates on Substrate Revealed by Atomic Force Microscopy, *J. Phys. Chem. B* **108**, 2833–2838 (2004).

40. J. Valanciunaite, S. Bagdonas, G. Streckyte, and R. Rotomskis, Spectroscopic study of $TPPS_4$ nanostructures in the presence of bovine serum albumin, *Photochem. Photobiol. Sci.* **5**, 381–388 (2006).
41. S. Korposh, R. Selyanchyn, and S.-W. Lee, Nano-assembled thin film gas sensors. IV. Mass-sensitive monitoring of humidity using quartz crystal microbalance (QCM) electrodes, *Sens. Act. B* **147**, 599–606 (2010).
42. P. Billot, M. Couty, and P. Hosek, Application of ATR-UV Spectroscopy for Monitoring the Crystallisation of UV Absorbing and Nonabsorbing Molecules, *Organic Process Research & Development* **14**, 511–523 (2010).
43. Y. Moriya, T. Hasegawa, T. Okada, N. Ogawa, E. Kawai, K. Abe, M. Ogasawara, S. Kato, and S. Nakata, Analysis of Gibbs Monolayer Adsorbed at the Toluene/Water Interface by UV-Visible Partial Internal Reflection Spectrometry, *Anal. Chem*. **78**, 7850–7856 (2006).
44. S.-W. Lee, N. Takahara, S. Korposh, D.-H. Yang, K. Toko, and T. Kunitake, Nanoassembled Thin Film Gas Sensors. III. Sensitive Detection of Amine Odors Using TiO_2/ Poly(acrylic acid) Ultrathin Film Quartz Crystal Microbalance Sensors, *Anal. Chem*. **82**, 2228–2236 (2010).

Cranfield University

CERES https://dspace.lib.cranfield.ac.uk

School of Aerospace, Transport and Manufacturing (SATM) Staff publications (SATM)

2017-11-09

Porphyrin-nanoassembled fiber-optic gas sensor fabrication: Optimization of parameters for sensitive ammonia gas detection

Korposh, Sergiy

Elsevier

Korposh S, Kodaira S, Selyanchyn R, et al., (2018) Porphyrin-nanoassembled fiber-optic gas sensor fabrication: optimization of parameters for sensitive ammonia gas detection. Optics & Laser Technology, Volume 101, May 2018, pp. 1-10

http://dx.doi.org/10.1016/j.optlastec.2017.10.027

Downloaded from Cranfield Library Services E-Repository